

Numerical analysis of a three-wave-mixing Josephson traveling-wave parametric amplifier with engineered dispersion loadings

Victor Gaydamachenko, Christoph Kissling, Ralf Dolata, and Alexander B. Zorin
Physikalisch-Technische Bundesanstalt, Bundesallee 100, 38116 Braunschweig, Germany

(*Electronic mail: victor.gaydamachenko@ptb.de, christoph.kissling@ptb.de)

(Dated: September 23, 2022)

The recently proposed Josephson traveling-wave parametric amplifier (JTWPA) based on a ladder transmission line consisting of radio-frequency SQUIDs and exploiting three-wave mixing (3WM), has great potential in achieving both a gain of 20 dB and a flat bandwidth of at least 4 GHz. To realize this concept in practical amplifiers we model the advanced JTWPA circuit with periodic modulation of the circuit parameters (engineered dispersion loadings), which allow the basic mixing process, i.e., $\omega_s = \omega_p - \omega_i$, where ω_s , ω_p , and ω_i are the signal, the pump, and the idler frequencies, respectively, and efficiently suppress propagation of unwanted higher tones including $\omega_{2p} = 2\omega_p$, $\omega_{p+s} = \omega_p + \omega_s$, $\omega_{p+i} = \omega_p + \omega_i$, etc. The engineered dispersion loadings allow achieving sufficiently wide 3 dB-bandwidth from 3 GHz to 9 GHz combined with a reasonably small ripple (± 2 dB) in the gain-versus-frequency dependence.

I. INTRODUCTION

Due to attainable quantum-limited performance, Josephson parametric amplifiers (JPAs) make a multitude of microwave quantum experiments possible, e.g., amplification and squeezing of zero-point fluctuations^{1,2}, dramatic improvement of sensitivity of quantum sensors³, observation of quantum jumps⁴, generation of entangled microwave radiation⁵, single-shot⁶ and continuous nondemolition⁷ measurements of superconducting qubits, etc. Nowadays they are considered as indispensable tools for quantum technologies⁸. Recently, Josephson *traveling-wave* parametric amplifiers (JTWPAs)^{9–20} are in particular focus of research in the fields of quantum communication and quantum computing. Thanks to their transmission-line architecture, leaving off a customary cavity, JTWPAs achieve a substantially wider bandwidth and larger dynamic range¹⁰.

The core of a JTWPA is a nonlinear microwave transmission line, made up of a LC-ladder circuit with cells, which include either single Josephson junctions (see, e.g., Refs.^{9–12}) or SQUIDs (see, e.g., Refs.^{13–21}). Due to their nonlinear current-phase relation (or, equivalently, nonlinear Josephson inductance L_J) these elements enable frequency mixing. The conventional scheme of JTWPAs^{9–13,19,20} is based on four-wave mixing (4WM), where frequencies of the signal, ω_s , the pump, ω_p , and the idler, ω_i , obey the relation $\omega_s + \omega_i = 2\omega_p$. Such mixing is enabled by the Kerr-like nonlinearity of the inverse Josephson inductance, $L_J^{-1}(\phi) \approx (1 - \gamma\phi^2)L_{J0}^{-1}$ with coefficient $\gamma = 1/6$, which stems from the Taylor-series expansion of the sine-shape current-phase relation of the Josephson current, $I = I_c \sin \phi$ ²². Here I_c is the critical current, $L_{J0}^{-1} = [\partial I(\phi)/\partial(\phi_0\phi)]_{\phi=0} = I_c/\phi_0$ is the inverse Josephson inductance for vanishingly small signals, and $\phi_0 = \hbar/2e$ is the reduced magnetic flux quantum.

The major challenge in designing JTWPAs with 4WM is fulfilling the matching relation for the corresponding wave numbers, $k_s + k_i = 2k_p$, in the range of operating frequencies and powers. The problem originates from the properties of the Kerr effect which, on the one hand, ensures 4WM, but, on the other hand, causes unwanted self-phase modulation (SPM)

and cross-phase modulation (XPM) of the waves due to the intensity-dependent refractive index of the line. This effect leads to imperfect phase matching, $\Delta k = 2k_p - k_s - k_i \neq 0$, which in addition is very sensitive to pump power²³. This problem of amplifiers with 4WM can be fixed by careful dispersion engineering, either by applying the resonant phase matching technique^{10–12}, where resonators are inserted into the transmission line at regular intervals, or by using periodic loadings in the transmission line, opening stop-bands in the dispersion relation¹⁹. In this way the phase velocity of the pump wave is adjusted yielding $\Delta k \rightarrow 0$. However, both techniques lead to a wide stop-band in the center of the gain profile. A recently demonstrated approach circumvents the need of dispersion engineering by reversing the sign of the Kerr nonlinearity, such that the nonlinear Kerr-induced phase shift compensates the linear dispersion phase mismatch^{13,20}. Although this elegant approach overcomes the problem of a stop-band in the gain profile, its gain profile is rather camel-back shaped than being flat.

Recently, the concept of a JTWPA with three-wave-mixing (3WM) was proposed¹⁴ and tested^{15,17}. In amplifiers of this type, the frequencies obey the basic parametric relation, $\omega_s + \omega_i = \omega_p$, and their mixing is possible due to the non-centrosymmetric nonlinearity of type^{24,25}

$$L_S^{-1}(\phi) \approx (1 - \beta'\phi)L_{S0}^{-1}, \quad (1)$$

where β' is the coefficient of the non-centrosymmetric nonlinearity, and L_S and L_{S0} denote the inductance for finite and vanishingly small signals, respectively. Such a nonlinearity can be engineered, for example, with the help of a flux-biased non-hysteretic rf-SQUID¹⁴. Alternatively, this nonlinearity can be engineered by using a modified (multi-junction) rf-SQUID having a Josephson kinetic inductance instead of linear inductance in one branch, i.e., the so-called superconducting nonlinear asymmetric inductive element (SNAIL)^{15,26–28}. Fine tuning of the bias flux allows full suppression of the Kerr nonlinearity in both rf SQUIDs and SNAILS.

Compared to the Kerr-based JTWPA with 4WM, the JTWPA with 3WM normally contains only a small or even vanishing Kerr-like nonlinearity, so it is almost free of SPM

and XPM effects²³ and the corresponding wave numbers k_s , k_i and k_p do not depend on the pump power. Although this remarkable property intrinsically ensures phase-matching for the basic 3WM process,

$$\Delta k = k_p - k_s - k_i \approx 0 \quad (2)$$

(naturally, in case of sufficiently small chromatic dispersion)¹⁴, the phase-matching conditions for unwanted mixing processes with higher frequencies are also satisfied. These processes include, e.g., the generation of the second harmonic of the pump, $\omega_{2p} = 2\omega_p$, and the sum-frequency generations, $\omega_{p+s} = \omega_p + \omega_s$ and $\omega_{p+i} = \omega_p + \omega_i$. All these unwanted mixing processes cause leakage of the pump power^{11,14} and dramatically limit the achievable signal gain²⁹. In fact, the amplitudes of these tones can be of the same order as pump and signal, respectively²⁹. This problem can be solved by engineering a relatively strong dispersion in the transmission line to break the phase-matching condition for all unwanted processes^{21,30,31}. This can be done, for example, by lowering the SQUID plasma frequency^{18,21}. At the same time, the phase-matching of the relevant 3WM process can be retained by techniques like resonant-phase-matching¹⁰ or quasi-phase-matching²¹. In this paper, however, we show how periodic dispersion loadings in the transmission line can be engineered such that the problem of unwanted mixing processes is solved and simultaneously the bandwidth and flatness of the resulting gain profile is maximized without change of the circuit architecture.

II. CIRCUIT DESCRIPTION

The electric diagram of our superconducting microwave circuit with nominally vanishing losses is shown in Fig. 1a.

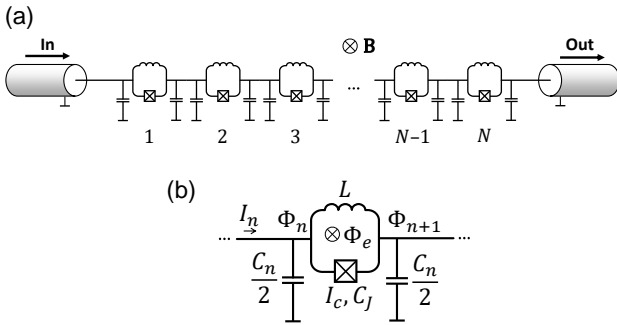


Figure 1. (a) Electric diagram of the JTWPA consisting of a serial array of $N \gg 1$ identical rf-SQUIDS with not necessarily identical ground capacitances C_n . Homogeneous magnetic field \mathbf{B} is perpendicular to the circuit plane and produces, as shown in panel (b), similar constant flux Φ_e applied to each rf-SQUID having inductance L and a Josephson junction with critical current I_c and self-capacitance C_J . The basic circuit variables are Φ_n , the flux value on the n -th node of the line, and I_n , the alternating current generated by a microwave and injected in the n -th rf-SQUID.

The circuit consists of an array of N elementary cells (see Fig. 1b). Each elementary π -type unit cell consists of an rf-SQUID, deployed as a nonlinear inductance enabling 3WM¹⁴, and two capacitances to ground $0.5C_n$ (with integer $n = 1 \dots N$), which are periodically varied to create the dispersion loadings. All N rf-SQUIDS, consisting of an inductance L in parallel to a Josephson junction having critical current I_c and junction capacitance C_J , are nominally identical and nonhysteretic, i.e., the dimensionless screening parameter $\beta_L \equiv LI_c/\phi_0 < 1$ ³².

For a vanishingly small ac current I injected in the rf-SQUID the *linear* inductance equals

$$L_S(I \rightarrow 0) \equiv L_{S0} = L / (1 + \beta_L \cos \phi_{dc}), \quad (3)$$

where the phase ϕ_{dc} is set by an external magnetic flux Φ_e ¹⁴. Thus, the inductance of the rf-SQUIDS can be effectively controlled *in situ* by a magnetic field \mathbf{B} , which is applied equally to all rf-SQUIDS, or alternatively, by injecting a dc bias current I_{dc} into the transmission line, and thus inducing $\Phi_e = LI_{dc}$.

Considering now a small but not vanishing ac phase perturbation $\phi = (\Phi_n - \Phi_{n+1})/\phi_0$ on the n -th rf-SQUID, induced by small injected ac current $I \ll \Phi_0/L_{S0}$, we find the inverse *nonlinear* SQUID inductance

$$L_S^{-1} = \frac{\partial I(\phi)}{\partial(\phi \phi_0)} \approx (1 - 2\beta\phi - 3\gamma\phi^2)L_{S0}^{-1}, \quad (4)$$

with β and γ denoting the coefficients of the non-centrosymmetric and the Kerr-nonlinearity, respectively. The coefficients β and γ ,

$$\beta = \frac{\beta_L}{2} \frac{\sin \phi_{dc}}{1 + \beta_L \cos \phi_{dc}}, \quad (5)$$

$$\gamma = \frac{\beta_L}{6} \frac{\cos \phi_{dc}}{1 + \beta_L \cos \phi_{dc}}, \quad (6)$$

are odd and even 2π -periodic functions of the phase ϕ_{dc} , respectively. Thus, the nonlinearity of the SQUID inductance is effectively controllable by Φ_e , too. Since 3WM is enabled by the non-centrosymmetric nonlinearity, we aim at a relatively large value of β . To reduce unwanted Kerr effects causing SPM and XPM, γ should be small. In this paper, we bias the SQUIDS by I_{dc} such, that $\phi_{dc} \approx \pi/2 + \beta_L$, for which β is close to its maximum value, and γ is sufficiently small, so that SPM and XPM do not cause substantial phase mismatch.

The nominal value of the inductance L and the average value of the ground capacitances

$$\bar{C} = \frac{1}{m} \sum_{n=1}^m C_n, \quad (7)$$

are chosen such that the characteristic impedance of the equivalent uniform transmission line for sufficiently low frequencies,

$$Z \approx \bar{Z} = \sqrt{\frac{L_{S0}}{\bar{C}}} = \sqrt{\frac{L}{\bar{C}(1 + \beta_L \cos \phi_{dc})}}, \quad (8)$$

is equal to $Z_0 = 50\Omega$ at the envisaged operation point ϕ_{dc} to achieve impedance-matching to the amplifier's experimental

environment. Note that this impedance can be in-situ flux-tuned.

The self-capacitance C_J of the Josephson junction yields the plasma frequency of the rf SQUID $\omega_J = (L_{S0}C_J)^{-1/2}$, and the ground capacitances define the characteristic frequency $\omega_0 = (L_{S0}\bar{C})^{-1/2}$, both constituting the cutoff frequency²⁹

$$\omega_c = 2(L_{S0}(\bar{C} + 4C_J))^{-1/2} = (\omega_0^{-2}/4 + \omega_J^{-2})^{-1/2} \quad (9)$$

No propagation of electromagnetic waves along the transmission line is possible for $\omega > \omega_c$. For lower frequencies, the transmission line becomes dispersive, and the dispersion relation $k(\omega)$ is approximately

$$k \approx \frac{\omega}{\omega_0} \left(1 + \frac{\omega^2}{2\omega_J^2} + \frac{\omega^2}{24\omega_0^2} \right) \quad (10)$$

for frequencies $\omega \ll \omega_0, \omega_J$. Here, the wave number k is normalized to the reverse physical size of the elementary cell d^{-1} ($d = \ell/N$, where ℓ is the total length of the line). Since typical signal, idler, and pump frequencies (e.g., $\omega_{s,i}/2\pi \approx 4\text{...}8$ GHz and $\omega_p/2\pi \approx 12$ GHz) are much smaller than both the frequencies $\omega_{0,J}/2\pi \approx 80\text{...}100$ GHz, the dispersion relation is roughly linear, $k \approx \omega/\omega_0$. Therefore, for the 3WM process, with $\omega_p = \omega_s + \omega_i$, the phase matching condition $k_p \approx k_s + k_i$ is approximately fulfilled. However, due to the almost linear dispersion relation, the phase matching conditions for *unwanted* 3WM processes, e.g.,

$$\omega_{p+s} = \omega_p + \omega_s, \quad k_{p+s} \approx k_p + k_s, \quad (11)$$

$$\omega_{p+i} = \omega_p + \omega_i, \quad k_{p+i} \approx k_p + k_i, \quad (12)$$

$$\omega_{2p} = 2\omega_p, \quad k_{2p} \approx 2k_p, \quad (13)$$

are roughly fulfilled, too. These processes are unwanted since they lead to leakage of power and undulations of the signal gain^{18,33} (c.f. Appendix A). It was shown recently via circuit simulations²⁹ that indeed a large number of unwanted mixing processes take place in a 3WM-JTWPA with a homogeneous transmission line and relatively low chromatic dispersion ($f_J = \omega_J/2\pi = 86$ GHz, $f_0 = \omega_0/2\pi = 67$ GHz), and that the gain in such an amplifier was thereby limited to rather smaller values on the order of 10 dB.

III. DISPERSION ENGINEERING

It is the major task in the design of a 3WM-JTWPA to destroy the phase-matching in all unwanted processes Eq. (11)–(13), while preserving it solely for the basic 3WM process Eq. (2). Our approach to tackle this issue is based on periodic dispersion loadings, which has the advantage that no modification of the circuit architecture is required (like, for example, inserting resonator-based phase-shifters into the transmission-line^{11,12}), but only a variation of the circuit parameters is needed.

The method of periodic dispersion loading has earlier been applied for 4WM traveling-wave amplifiers, based on the non-linearity of the kinetic inductance (KI-TWPAs) and designed

as a superconducting coplanar waveguide transmission line³⁴. The engineered loadings were realized as waveguide regions of certain length with increased width. Placed at specific intervals, these loadings formed a frequency stop band and thus prevented propagation of unwanted waves (e.g., the third harmonic of the pump generated due to the Kerr nonlinearity). KI-TWPAs with additional dc biasing enabling both 4WM and 3WM^{30,35} were realized using similar concepts. In their analysis of periodic loadings in KI-TWPA, Erickson and Pappas³⁶ suggested that this method may also be applicable to the lumped-element (Josephson-junction based) traveling-wave parametric amplifiers. This concept was demonstrated recently by Planat et al.¹⁹ for a 4WM-JTWPA. In this paper we extend the concept of periodic loadings to the case of a 3WM-JTWPA based on an rf-SQUID array.

In our approach, the periodic loadings are realized by variation of ground capacitances C_n . The periodic variation of the ground capacitances leads to a corresponding modulation of the local value of phase velocity, $v_n = d/\sqrt{L_{S0}C_n}$, with a shape similar to that in the Kronig-Penney model³⁷. The wave frequency $\omega(k)$, as a function of (Bloch) wave number k , forms in this case a band structure with opened gaps (frequency bands of forbidden wave propagation) at $k_j = jk_m/2$, where $k_m = 2\pi/m$, and centered around frequencies $\omega_j = (j\pi/m)\omega_0$, where integer m is the period of the capacitance variation and integer variable $j = 1, 2$, etc. The size of the j -th gap is proportional to the corresponding j -th Fourier coefficient in the expansion of the Kronig-Penney potential³⁸.

Our periodic loadings are designed such that the first gap ($j = 1$) of the resulting band structure $\omega(k)$ is rather narrow and the second gap ($j = 2$) is wide. This is achieved using a variation of the ground capacitances C_n with three discrete capacitances as shown in Fig. 2a. This modified Kronig-Penney waveform³⁷ has a basic period of m or, equivalently, the dimensionless space frequency of $k_m/2\pi = 1/m$. However, the double-frequency component $2/m$ of this waveform (corresponding to the period of $m/2$) has substantially larger modulation depth than that of the basic frequency $1/m$. This relation is due to inserting two slightly different capacitances for each half-period. Therefore, the width of the second gap in the spectrum $\omega(k)$ is expected to be notably larger than that of the first gap. The shape of $\omega(k)$ can be calculated analytically using the transfer-matrix-method (TMM)³⁹, as described in Appendix B, and is presented in Fig. 2b.

The purpose of the narrow first gap is preserving optimal phase-matching for the basic 3WM process, while the wide second gap is used for suppressing higher-frequency mixing modes. The former is necessary because of a non-negligible phase-mismatch $\Delta k > 0$, which is a side-effect of the wide gap $j = 2$. This mismatch corresponds to a coherence length $\xi = \pi/\Delta k$ on the order of a few hundred elementary cells, $\xi < N$, limiting the achievable signal gain. However, placing the pump frequency ω_p slightly above the upper edge of the first gap makes it possible to somewhat reduce the wave number k_p and, hence, compensate the mismatch Eq. (2), $\Delta k \approx 0$, in a rather wide range of the signal frequency (Fig. 2c). This corresponds to a coherence length ξ on the order of several thousands of elementary cells, and for $\xi \gg N$ it results in

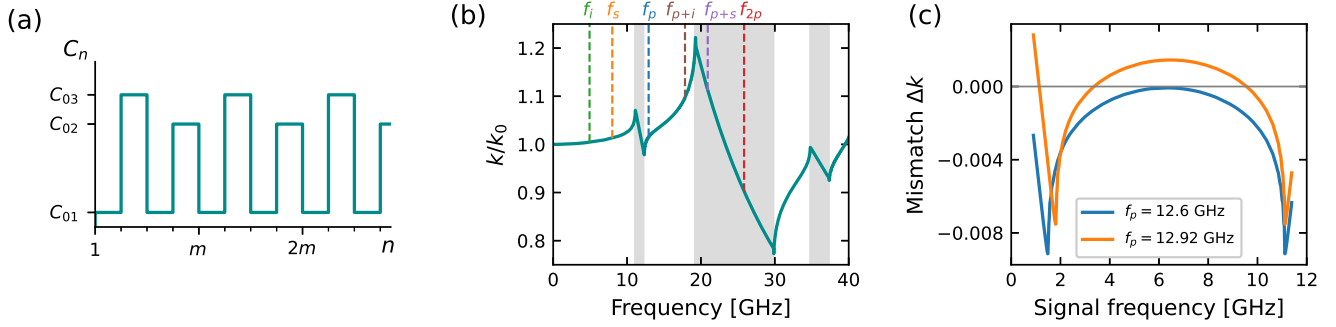


Figure 2. Dispersion engineering via periodic loadings. (a) Scheme of periodic variation of the ground capacitance C_n over the length of the JTWPA transmission line. The values of ground capacitances C_n , $n = 1, 2, \dots, N$, are altered between three constant values, with the global period m . It is assumed that $0.25m$ is an integer and, for example, the first segment with $C_n = C_{01}$ extends from $n = 1$ up to $n = 0.25m$ inclusively. (b) Resulting dispersion relation, normalized on $k_0 = \omega/\omega_0$. Grey-shaded areas denote stop-bands (gaps), opened due to the periodic loadings shown in panel (a). The pump frequency is fixed at the upper edge of the first gap (corresponding to loading period m) so that k_p is lowered and phase-matching of the pump, the signal, and the idler is achieved. All unwanted higher-frequency tones, f_{p+} , f_{p+i} , f_{2p} , etc., are strongly phase-mismatched since they fall either into the highly dispersive region above f_p or into the wide second gap (corresponding to loading period $m/2$). The position of the six most relevant 3WM tones are marked by vertical dashed lines for the case of $f_p = 12.92$ GHz and $f_s = 8$ GHz. (c) Phase-mismatch $\Delta k = k_p - k_s - k_i$ versus f_s for two different pump frequencies. Plots in (b) and (c) are calculated using TMM for the circuit parameters $C_{01} = 8.8$ fF, $C_{02} = 62.3$ fF, $C_{03} = 80$ fF, $m = 20$, $L_{s0} = 109$ pH, $C_J = 20$ fF, and $N = 1500$.

nearly exponential signal growth along the array¹⁴.

The wide second gap encompasses the second harmonic of the pump, ω_{2p} , and covers a wide frequency range around this frequency (see Fig. 2b). The up-converted frequencies ω_{p+} and ω_{p+i} either also fall in this gap or are located near the band edge (purple and brown dashed lines in Fig. 2b). Then either the propagation of the generated waves is forbidden, or the phase matching for the corresponding processes, given by Eqs. (11)-(13), is violated. The latter condition prevents a steady amplification of the respective wave, so these tones can only grow in an undulation manner. In this way, it is quite possible to effectively suppress the growth of unwanted mixing modes, while preserving the phase-matching of the basic 3WM process.

IV. CIRCUIT SIMULATIONS

A. WRspice circuit model

In order to numerically model our JTWPA circuit, we use the software *WRspice*⁴⁰, which is a SPICE-based circuit simulator, capable of simulating circuits containing Josephson junctions. *WRspice* has been used earlier to model the JTWPA without dispersion engineering of the transmission line based on rf-SQUIDS²⁹ and for analyzing the effect of parameter variation on the performance of this JTWPA⁴¹. Compared to other approaches of analyzing a JTWPA, SPICE simulations offer more flexibility in modeling and rigorously analyzing the circuit – an advantage which comes at the cost of higher computation power. The alternative coupled-mode equations (CME) approach, often used to analyze JTWPAs^{9,10,34}, gives valuable insight into the physics of such devices, but relies

on several assumptions and approximations, including the transition from the discrete to the continuous telegrapher's equation⁹, the slowly-varying amplitude approximation¹⁰, and the restriction to a limited number of tones included in the analysis²⁹. The approach of Planat et al.¹⁹, based on finding the solution of the discrete wave equation in the form of traveling waves, avoids most of these approximations, but does not allow including reflections of the pump wave (below we show that for our circuit the pump reflections can be quite pronounced). Moreover, it is a commonly applied approximation to omit higher orders of nonlinearity of the examined device in its theoretical description (c.f. the truncated Taylor series in Eq. (4)). In contrast to these approaches, no such assumptions are made in a *WRspice* transient analysis. Specifically, *WRspice* simulator models the conventional sinusoidal current-phase relation of the Josephson junction and thus synthesizes the current-phase relation of rf-SQUIDs in a form which Taylor expansion also contains infinite number of terms. In this way, the simulator takes into account all waves occurring due to high-order nonlinearities and their reflections.

The JTWPA circuit model and its parameters used throughout this paper are presented in Fig. 3a. In our model, Josephson junctions obey the RCSJ model^{42,43} with critical current I_c , junction self-capacitance C_J , and a linear subgap resistance R_J , modeling the quasiparticle losses in the Josephson junctions. The subgap resistance causes an attenuation⁴⁴

$$A [dB] = 10 \log_{10}(e) N \omega^2 L_{s0}^2 / Z_0 R_J, \quad (14)$$

which amounts to ca. 1 dB at 13 GHz. The junction gap voltage, $V_g = 2.6$ mV (typical value for Nb), has no influence on the results of the simulations presented in this paper, because the Josephson junctions always remain in the superconducting state, while the microwave oscillations of the phase are small.

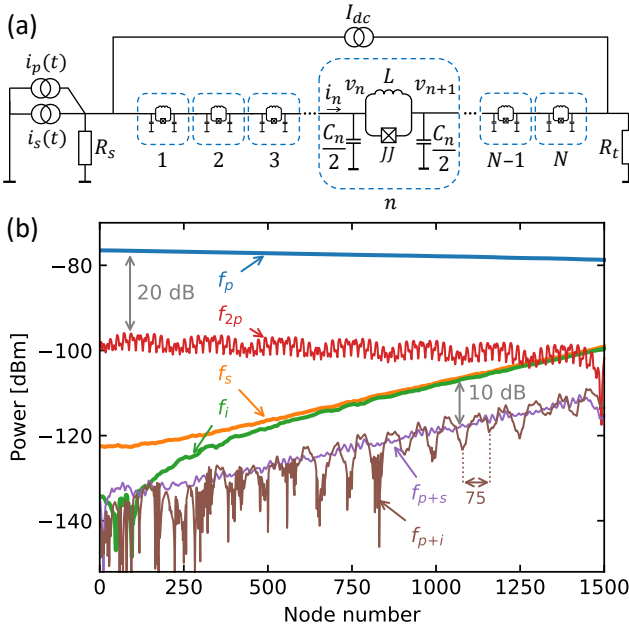


Figure 3. (a) Schematic of the JTWPA circuit implemented in simulator *WRspice*. The circuit consists of $N = 1500$ π -type unit cells, having capacitances C_n according to the capacitance profile of Fig. 2a, and inductances $L = 84$ pH. The Josephson junction (JJ) obeys a RCSJ model as described in the text, with $I_c = 1.57$ μ A, $C_J = 20$ fF, and $I_c R_J = 16.5$ mV. Input and output of the circuit are terminated by resistances $R_s = R_t = 50$ Ω , respectively. Pump and signal are fed by current sources with currents $i_p(t) = \hat{i}_p \sin \omega_p t$ and $i_s(t) = \hat{i}_s \sin \omega_s t$, respectively; a dc current $I_{dc} = 9.8$ μ A provides the flux-biasing of all rf-SQUIDS. Panel (b) shows the propagation of the six most relevant waves along the JTWPA extracted from the *WRspice* simulation. The unwanted higher-frequency tones f_{2p} , f_{p+} , and f_{p+i} are significantly suppressed. All higher harmonics and mixing products had notably lower powers than the latter three tones. The signal and idler tones rise nearly exponentially, demonstrating an almost pure 3WM process. Parameters of the circuit used in this simulation are $\hat{i}_p = 2.0$ μ A, $f_p = 12.92$ GHz, and $f_s = 6.7$ GHz. The signal level, $\hat{i}_s = 0.01$ μ A, was sufficiently low, so that the amplifier saturation for the given gain of ca. 20 dB remained negligibly small.

Other passive circuit components (inductances L and capacitances C_n) are modelled as lumped and lossless components. A transient analysis computes voltages $v_n(t)$ and currents $i_n(t)$ for each node n as a function of time over a specified time interval. These transient quantities are then converted to the frequency domain performing Discrete Fourier Transform (see Appendix C for details) and the amplitudes and phases of the relevant tones are extracted.

B. Wave-mixing and parametric amplification

The spatial evolution of the waves of the principal tones, i.e., pump f_p , signal f_s , and idler f_i , plus the undesired waves with frequencies f_{p+} , f_{p+i} , and f_{2p} , are shown in Fig. 3.

For each of these tones, the powers $P_n = \frac{1}{2} \text{Re}\{V_n I_n^*\}$ associated with the n -th node (V_n is the complex node voltage in the frequency domain, I_n^* is the complex-conjugate of the complex node current I_n), are plotted against the node number. One can see that the signal and the idler increase almost exponentially¹⁴,

$$A_s(n) \propto \cosh(gn) + \frac{i\Delta k}{2g} \sinh(gn), \quad (15)$$

$$A_i(n) \propto \sinh(gn), \quad (16)$$

as they propagate along the array. Here, A_s, A_i are the (complex) amplitudes of the signal and the idler, respectively, and g is an exponential gain coefficient¹⁴. This gives evidence of parametric amplification with almost pure 3WM, remaining phase-matched all along the line, with a coherence length $\xi = 2186 > N$, and resulting in a signal gain of ca. 22 dB for the frequencies given in the caption of Fig. 3b. In contrast, the mixing process given by Eq. (12) is mismatched, i.e,

$$\Delta k_{p+i} = k_{p+i} - k_p - k_i \gg \pi/N, \quad (17)$$

and thus it is incoherent, with $\xi_{p+i} = \pi/\Delta k_{p+i} = 75 \ll N$ (brown line). The tones f_{p+} (purple line) and f_{2p} (red line) are evanescent modes³⁶, i.e., they fall in the wide second gap, where no propagation is possible, and show distinct beating patterns. For example, the tone f_{2p} appears as two predominant superimposed beating patterns with envelope periods of $\pi/(2k_p - k_m) = 104$ cells each. The up-conversion tones, f_{p+} and f_{p+i} , are each ca. 10 dB lower in amplitude than the signal, and the power of the second harmonic of the pump is about 20 dB below the pump wave power. Hence these tones are strongly suppressed. For example, only ca. 1% of the pump power is converted to harmonics (all higher harmonics have even lower amplitudes than the second harmonic). For comparison, in a JTWPA circuit without dispersion engineering (with otherwise identical circuit parameters) up to 70% of the pump power is converted to harmonics (see Appendix A).

C. Gain profile

Continuous broadband gain was found only for pump frequencies slightly above the first gap. Pump frequencies in a range of roughly 12.4–13.2 GHz permit sufficient phase matching for broadband signal gain of $G = |S_{21}|^2 > 20$ dB at $\hat{i}_p = 1.8$ μ A (incident pump power $P_{p,in} \approx -78$ dBm). Varying the pump frequency alters $\Delta k(f_s)$ (see Fig. 2c) and thus influences the shape of the gain profile. The dependence of the gain on the signal frequency is shown in Fig. 4 for two different pump frequencies. The gain profile for $f_p = 12.48$ GHz shows a nearly elliptical shape, since the phases of pump, signal, and idler are matched best in the center of the signal band, $f_s = f_p/2$. For $f_p = 12.92$ GHz, phase-matching is imperfect in the center, but perfect ($\Delta k = 0$) farther apart from the center (see the orange curve in Fig. 2c). This leads to a slight drop in the center of the gain profile, when compared to that for $f_p = 12.48$ GHz, but also to better flatness and larger 3 dB-bandwidth of ca. 7.2 GHz $\approx 0.56 f_p$. The resulting band-

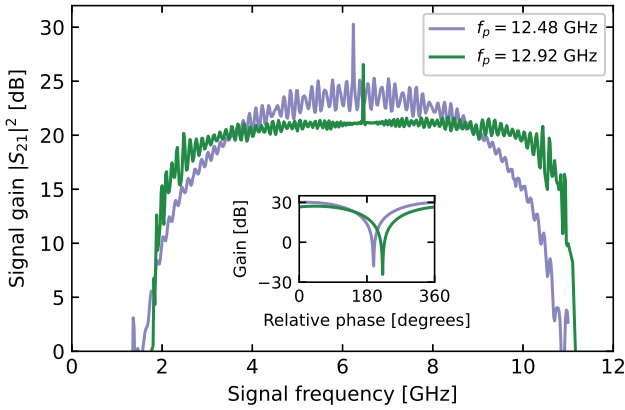


Figure 4. Signal gain versus frequency in a JTWPA for two different pump frequencies. While higher gain $|S_{21}|^2$ is obtained with $f_p = 12.48$ GHz, the pump frequency $f_p = 12.92$ GHz yields better flatness, larger 3 dB-bandwidth, and greatly reduced ripple. The peaks in the center of the curves occur due to degenerate 3WM, i.e., $f_s = f_i = f_p/2$. In this regime, parametric amplification is phase-sensitive. The inset shows the phase-sensitivity of the gain at $f_s = f_p/2$, where the signal phase was tuned relative to the phase of the pump. The phase-sensitive gain varies periodically between amplification and deamplification. In the case of deamplification the gain profile would show a dip in its center. The maximum degenerate gain is ca. 6 dB higher than the nondegenerate gain in the vicinity of $f_p/2$, while the maximum extinction ratio is approaching 48 dB for $f_p = 12.48$ GHz and 51 dB for $f_p = 12.92$ GHz. The pump amplitude was $\hat{I}_p = 1.8 \mu\text{A}$ in these simulations.

width is furthermore a function of the convexity of the dispersion relation³⁰, which is defined by the width of the gaps or, equivalently, the modulation depth of the capacitance profile C_n . A smaller modulation depth leads to a wider range of phase-matched signal frequencies, but also reduces the phase-mismatch for unwanted processes. Thus the modulation depth is a tradeoff between bandwidth and the suppression of unwanted parametric processes.

The distinct peaks at $f_s = 6.24$ GHz and 6.46 GHz for $f_p = 12.48$ GHz and 12.92 GHz, respectively, emerge due to degenerate 3WM, where the signal and idler frequencies coincide, $f_s = f_i = f_p/2$. As long as the phase of the idler is rigidly connected to the phases of the pump and the signal (see, e.g., Eq. (19) in Ref.¹⁴), the signal and the idler interfere either constructively (leading to amplification) or destructively (leading to deamplification), depending on the phase of the signal relative to that of the pump. Respective simulations are shown in the inset in Fig. 4. This interesting regime, where single-mode squeezing is possible³¹, is easily accessible in a 3WM-JTWPA, since the pump frequency is well separated from the signal and the idler, $f_p = 2f_{s,i}$ (in contrast to a conventional 4WM-JTWPA, where the signal and the idler coincide with the strong pump tone, $f_p = f_{s,i}$, that masks the effect). As was recently demonstrated by Qiu et al.⁴⁵, phase-sensitive amplification is, however, possible using two pump waves ($f_{p1} < f_s = f_i < f_{p2}$) in a 4WM-JTWPA, and they re-

port a a large extinction ratio of 56 dB.

The ripple in the gain profile (Fig. 4) is an unwanted but expected feature for any JTWPA with a slight impedance mismatch $Z \neq Z_0$ (Z_0 is the impedance of the external circuit connected to the JTWPA)^{19,33,34}. For the curves in Fig. 4 the average value $\bar{Z} = 52 \Omega$ (valid for low frequencies, i.e., wavelengths $\gg m$) is close to Z_0 . The impedance mismatch is in this case mainly caused by the frequency dependence of Z due to relatively low frequencies f_J and f_0 and significant dispersion in the range from 0 to f_p engineered by the periodic loadings. This impedance mismatch causes signal reflections at both ends of the array, and the back- and forth-propagating signal wave creates a Fabry-Perot-like interference pattern¹⁹. The frequency-spacing in this pattern corresponds to twice the electrical length of the array, $\Delta f = v_p/2\ell \approx \omega_0/2N = 160$ MHz, where v_p is the average phase velocity. The idler wave is also multiply reflected, but travels at a slightly different phase velocity due to small chromatic dispersion. The parametric interaction of signal and idler between their multiple reflections leads to ripple having two superimposed, slightly different, periods. Furthermore, it was observed in simulations (not shown) that the amount of ripple increases with increasing gain, which is a fingerprint of Fabry-Perot-like interferences in JTWPAs due to the amplification the signal wave experiences as it travels between its multiple reflections¹⁹. In the same way, the occurrence of backward amplification, i.e., the 3WM interaction of the reflected signal (wave-number $-k_s$) with the reflected pump ($-k_p$)³³, can further enhance ripple. For pump frequencies closer to the gap the reflectivity and hence the backward gain are high (see inset in Fig. 5), which accounts for the higher amount of ripple in the gain profile of $f_p = 12.48$ GHz compared to that of $f_p = 12.92$ GHz (Fig. 4).

To decrease ripple and prevent strong backward-traveling signal waves, the reflectivity at the output and the input of the array should be minimized for both the signal, say, between 1 and 11 GHz, and the pump frequency. Therefore, sufficiently good impedance matching should be achieved. The passive circuit components L and C_n , designed to meet the target value $Z = Z_0$ at the envisaged working point $\phi_{dc}^{\text{opt}}(\phi_e) \approx \pi/2 + \beta L$, can only be manufactured within certain technological margins. However, the dependence $Z(\phi_{dc})$ (Eq. (8)) is rather steep in the vicinity of that working point, such that small deviations of L and C_n from their target values can be compensated by fine-tuning of ϕ_e without degrading the amplifier performance dramatically. For example, $\Delta Z = \pm 10\%$ is achieved by $\Delta\phi_e \approx \pm 0.4$ rad. The corresponding change of β is smaller than 20%, which can be compensated by changing the pump amplitude. The Kerr coefficient, $|\gamma| < 0.08$, is still only a fraction of $|\beta|$, and the resulting phase-mismatch due to SPM and XPM can be compensated by re-adjusting the pump frequency anyway. Therefore, the circuit design allows *in-situ* fine tuning of the transmission line impedance by an external magnetic field and thereby makes it possible to reduce unwanted reflections of microwaves at the output and the input.

It is not possible, however, to fully suppress gain ripple by fine-tuning of the impedance. Due to the periodic variation of the ground capacitances, the impedance Z , with average

value \bar{Z} (valid only for wavelengths $\gg m$), shows a slight periodical variation with frequency. This variation appears as side-lobes of the gaps (being the main-lobes) in the reflection coefficient $S_{11}(f)$, which is presented in Fig. 5. The sidelobes have a periodicity of $\Delta f \approx \omega_0/2N = 160$ MHz, similar to that of the gain ripple. For frequencies closer to the gap this period is reduced. The gaps and their side-lobes shift slightly to smaller frequencies as the pump power is increased (inset in Fig. 5), which is due to a small residual Kerr nonlinearity¹⁹. This shift is small, however, when compared to that reported in Ref.¹⁹. To minimize pump reflections, the pump frequency is placed in the minimum between two adjacent side-lobes. In the signal band (ca. 3...9 GHz), sufficiently far below the first gap, the reflection coefficient of up to -19 dB is rather small, but still leads to weak multireflections, and thus to notable gain ripple (Fig. 4). When the average impedance is matched, $\bar{Z} = Z_0$, these side-lobes are the main cause of ripple in the gain profile. It should be noted that the occurrence of side-lobes is immanent to the concept of periodic loadings and cannot be resolved by standard impedance matching techniques easily. However, its effect can be possibly mitigated using the apodization technique, a well-established method for side-lobe suppression in optical fibre Bragg gratings^{46,47}. Adapting this technique to our concept should be possible by designing a non-uniform modulation depth of the periodic loadings (instead of a uniform modulation depth as in the present paper), enveloped by a suitable apodization function, e.g., a truncated Gaussian. Potentially this could be a method to strongly reduce unwanted reflections and ripple in the gain profile.

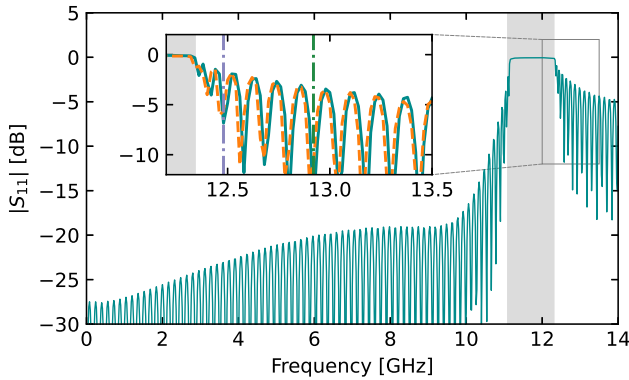


Figure 5. The reflection coefficient $|S_{11}|$ for typical frequencies of signal, idler, and pump. The quasi-periodic patterns are the side-lobes of the first stop-band (grey-shaded area). The inset shows a close-up view of $|S_{11}|$ in the pump frequency range. As the pump power increases ($\hat{I}_p = 0.01$ μ A for the cyan curves and $\hat{I}_p = 1.8$ μ A for the dashed orange curve), the gap and its side-lobes shift slightly to lower frequencies. To minimize pump reflection, the pump frequency is placed in a minimum between two adjacent side-lobes; violet and green vertical lines mark the pump frequencies used in Fig. 4. The curves are obtained by *WRspice* simulations where only one sine-wave (pump) current was injected ($\hat{I}_s = 0$).

V. CONCLUSION

In conclusion, we have proposed a modified design of a lumped-element Josephson traveling-wave parametric amplifier using periodic loadings with the shape shown in Fig. 2a and illustrated by circuit simulations the possibility to achieve gain of 20 dB in the frequency range from 3 GHz to 9 GHz. We presented a simulation approach which includes all occurring tones, reflections from the amplifier terminations, etc., and has no assumptions on the order of nonlinearities produced by the Josephson junctions. Our implementation of periodic loadings enables both reasonable phase matching of the basic 3WM process and effective suppression of unwanted high-frequency modes. The design of the device remains simple and close to the original design¹⁴, i.e., it does not need any additional elements in the amplifier architecture. Furthermore, it is possible to slightly tune the line impedance of the device by a magnetic flux bias. We believe that further improvement of the JTWPA characteristics is possible by applying periodic loadings with a more sophisticated design, including periodic variation of the rf-SQUID parameters. This could be done, for example, by varying the sizes of the Josephson junctions along the array according to the recently proposed technique of the Floquet-mode JTWPA⁴⁸.

We think that periodic loadings in JTWPAs with 3WM may open the way to practical low-noise parametric devices with sufficiently large bandwidth, which are a key enabling technology for quantum communication and quantum computing circuits. Due to good phase matching, a JTWPA of this type presents a circuit with remarkable properties, which may allow, for example, creating various quantum states of microwaves in a wide frequency range^{49,50}.

ACKNOWLEDGMENTS

The authors would like to thank Lukas Grünhaupt for useful discussions and Tom Dixon, Dominik Müller and Victor Rogalya for their assistance in setting up the simulator platform. This work has received funding from the EMPIR programme (project ParaWave 17FUN10) co-financed by the Participating States and from the European Union's Horizon 2020 research and innovation programme. This work was also supported by the German Federal Ministry of Education and Research (BMBF) within the framework programme “Quantum technologies – from basic research to market” (Grant No. 13N15949). C.K. gratefully acknowledges the support of the Braunschweig International Graduate School of Metrology B-IGSM and the DFG Research Training Group 1952 Metrology for Complex Nanosystems.

AUTHOR DECLARATIONS

Conflict of Interest

The authors have no conflicts to disclose.

Author Contributions

V. Gaydamachenko and **C. Kissling** contributed equally to this work.

V. Gaydamachenko: Investigation (equal); methodology (equal); software (equal); validation (equal); visualisation (equal); writing - original draft (equal). **C. Kissling:** Investigation (equal); formal analysis (lead); methodology (equal); software (equal); validation (equal); visualisation (equal); writing - original draft (equal). **R. Dolata:** Funding acquisition (lead); Project administration (lead); supervision (equal); writing - review & editing (supporting). **A. B. Zorin:** Conceptualization (lead); methodology (supporting); supervision (equal); writing - original draft (equal); writing - review & editing (lead).

DATA AVAILABILITY STATEMENT

The data that support the findings of this study are openly available in Zenodo repository at <https://doi.org/10.5281/zenodo.7092947>.

Appendix A: JTWPA without dispersion engineering

In a JTWPA without dispersion engineering, i.e., with a homogeneous transmission line, the signal gain is limited by power leakage from the main tones to unwanted tones. To il-

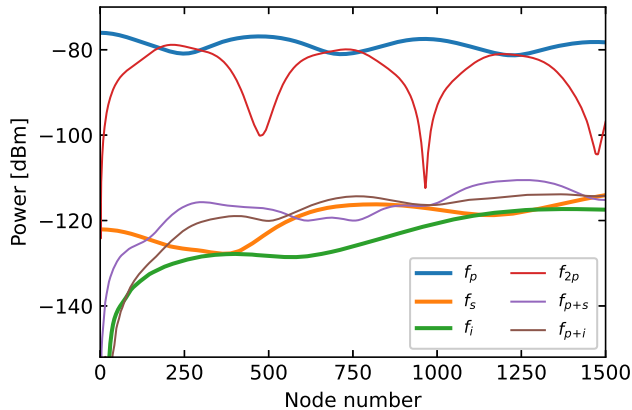


Figure 6. The dynamics of the major six waves propagating along the homogeneous JTWPA without dispersion engineering, i.e., having identical ground capacitors throughout the array. Power is transferred alternatingly between the pump and the second harmonic of the pump; and the pump is decreased in its minima by 5 dB, where the second harmonic power is larger than the pump power. The signal and idler waves cannot grow monotonically due to their strong interaction with the up-conversion tones f_{p+s} and f_{p+i} . The signal gain is 8 dB. Parameters used in this simulation are $\hat{I}_p = 2.0 \mu\text{A}$, $f_p = 12.92 \text{ GHz}$ and $f_s = 8.0 \text{ GHz}$, and the circuit parameters are as described in the text.

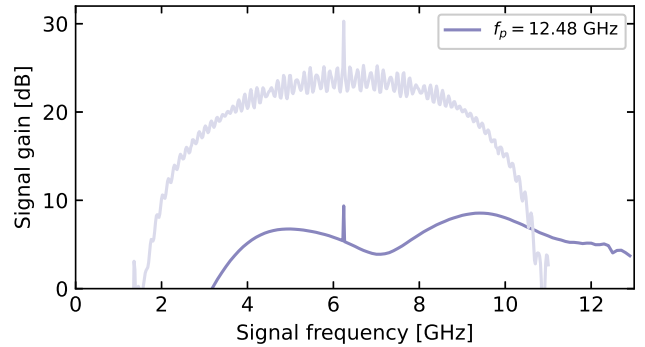


Figure 7. Signal gain versus frequency in the JTWPA without dispersion engineering (dark-purple curve). For comparison the respective curve of a dispersion-engineered JTWPA (light-purple curve, c.f. Fig. 4) is shown. Without dispersion engineering the signal gain is limited to ca. 9 dB and the gain profile is asymmetric. The distinctive peaks stem from the phase-sensitive amplification at the degenerate 3WM, $f_s = f_p/2$. The pump amplitude is $\hat{I}_p = 1.8 \mu\text{A}$ and the circuit parameters are as described in the text.

lustrate the benefit of our proposed dispersion engineering approach, we present here the circuit simulations of a homogeneous JTWPA circuit for comparison with Fig 3b and Fig. 4. For comparability, the circuit parameters were chosen identical to those of our proposed dispersion engineered JTWPA, apart from the homogeneous capacitance profile with constant ground capacitance values $C_n = \bar{C} = 40 \text{ fF}$ for all $n = 1 \dots N$. The resulting characteristic frequency ω_0 was identical to that of our proposed JTWPA circuit. The dispersion of this circuit, with the dispersion relation given by Eq. (10), is low in the frequency range $0 \dots f_{2p}$. Therefore, the phase mismatch of the second harmonic, $\Delta k_{2p} = k_{2p} - 2k_p$, is small, and the coherence length of the second harmonic, $\xi_{2p} = \pi/\Delta k_{2p}$, is on the order of 500 cells (see Fig. 6). This allows the second harmonic to grow to high amplitudes on the order of the pump amplitude, before the direction of power transfer reverses and power flows back to the pump wave. This power leakage to the second harmonic depletes the pump periodically to powers lower than 30% of its incident value $P_{p,in}$. Consequently, the average pump amplitude, needed for efficient parametric amplification, is significantly reduced.

Similar reasons allow a strong power transfer from the signal and the idler tones to the up-conversion tones f_{p+s} and f_{p+i} , whose amplitudes are either in the order of or even higher than the signal and idler amplitudes, respectively. These tones decimate the signal and the idler, so that an exponential growth of the signal is impossible and the gain is limited to rather small values of less than 10 dB (Fig. 7, compare with Fig. 8 in Ref.²⁹). Note that the signal wave shown by the orange line in Fig. 6 is less affected by up-conversion than the idler wave (green line). This is due to worse phase matching (shorter coherence length $\xi_{p+s} = 735$) than that of its counterpart ($\xi_{p+i} = 1402$) because of stronger dispersion at higher frequencies (Eq. (10)). This explains the asymmetry of the gain profile in Fig. 7.

Appendix B: Transfer-matrix method

The transfer-matrix method is a standard approach in optics³⁹ and microwave engineering⁴⁴ and is particularly useful for linear circuits consisting of cascaded two-ports. Here we apply this method to the JTWPA which is a cascade of N elementary two-ports shown in Fig. 1b. Each two-port n is described by a transfer matrix T_n (also referred to as ABCD-matrix)

$$T_n = \begin{pmatrix} A_n & B_n \\ C_n & D_n \end{pmatrix}, \quad (B1)$$

with the coefficients

$$A_n = 1 - \frac{1}{2} \frac{\omega^2 L_{S0} C_n}{1 - \omega^2 C_J L_{S0}}, \quad (B2)$$

$$B_n = \frac{i\omega L_{S0}}{1 - \omega^2 C_J L_{S0}}, \quad (B3)$$

$$C_n = i\omega C_n - \frac{1}{4} \frac{i\omega^3 L_{S0} C_n^2}{1 - \omega^2 C_J L_{S0}}, \quad (B4)$$

$$D_n = A_n \quad (B5)$$

These N transfer matrices T_n are then cascaded to a system transfer matrix

$$T_N = \begin{pmatrix} A & B \\ C & D \end{pmatrix} = (T_{01}^\kappa T_{02}^\mu T_{01}^\kappa T_{03}^\nu)^{\frac{N}{m}}, \quad (B6)$$

where the indices 01, 02, and 03 refer to the respective ground capacitor C_n (see Fig. 2a), the exponents κ, μ and ν are integers and denote the number of elementary two-ports of each variant (e.g., $\kappa = \mu = \nu = 5$ in our circuit) in one section, and in total there are N/m such cascaded sections, with $m = 2\kappa + \mu + \nu$. The system transfer matrix can then be transformed to a scattering matrix⁴⁴ for a given reference impedance Z_0 . The input reflection S_{11} and forward transmission S_{21} (for this linearized circuit $S_{12} = S_{21}$ and $S_{22} \approx S_{11}$) are given by the following expressions:

$$S_{11} = \frac{A + B/Z_0 - C Z_0 - D}{A + B/Z_0 + C Z_0 + D}, \quad (B7)$$

$$S_{21} = \frac{2}{A + B/Z_0 + C Z_0 + D}. \quad (B8)$$

Appendix C: Simulation setup and post processing

All simulations presented in this paper were performed by the open-source software *WRspice* as transient analysis. A *WRspice* netlist containing our JTWPA circuit can be found in Ref.⁵¹. As a default initial condition, internal routines of *WRspice* set all currents through inductors and all voltages across Josephson junctions to zero. In this way, the flux-phase relations in loops containing Josephson junctions are imposed⁴⁰. The dc bias current source is ramped up from zero to its final value of 9.8 μA within 0.4 ns to avoid large transients.

AC sources are active from the beginning of simulation. The transient response of the perturbation caused by the sources propagates and takes ca. $t_{tr} = \ell/v = N/\sqrt{L_{S0} C} = 3.13$ ns to reach the end of the circuit. The circuit is close to its steady state after 10 ns. Time domain data is saved between 10 ns and 60 ns, giving a total sampling time $T = 50$ ns, which defines the resolution of the Fourier transform $\Delta f = 1/T = 20$ MHz. Increasing the delay time of 10 ns does not change the results notably. The maximum time step of transient analysis is set to $\Delta t = 4.0$ ps. Note, that the maximum time step is chosen so small that the adaptive time step control of *WRspice* (automatically adapting the time step to optimize simulation time and accuracy) is overridden. Thus, the resulting time series is equidistant and Δt defines the maximum frequency of the Fourier transform, $f_{max} = 1/2\Delta t = 125$ GHz $> f_J, f_0$.

In the post processing the output of *WRspice*, the time-series of voltages $v_n(t)$ and currents $i_n(t)$ for each individual node n , is transformed to the frequency domain by applying a Discrete Fourier Transform (DFT). In our implementation the DFT is defined as

$$I_{q,n} = \frac{1}{M} \sum_{\tau=0}^{M-1} i_n \exp\left(-\frac{2\pi i}{M} \tau q\right), \quad q = 0, \dots, M-1, \quad (C1)$$

$$V_{q,n} = \frac{1}{M} \sum_{\tau=0}^{M-1} v_n \exp\left(-\frac{2\pi i}{M} \tau q\right), \quad q = 0, \dots, M-1. \quad (C2)$$

Here M is the size of the time-series and q is the index defining the corresponding frequencies $f_q = q\Delta f$. After DFT, we extract currents $I_n(f = f_j) = I_{j,n}$ and voltages $V_n(f = f_j) = V_{j,n}$ for each tone with index $j \in \{s, i, p, p+s, p+i, 2p\}$ and for each individual node n . We have chosen T such that all f_j coincide with a frequency sample $\tilde{q}\Delta f$, where $\tilde{q} \in \{0, \dots, M-1\}$.

Afterwards, the scattering parameters S_{11} and S_{21} can be generically calculated for a given frequency as follows:

$$S_{11} = \frac{V_{in} - Z_0 I_{in}}{V_{in} + Z_0 I_{in}} = \frac{Z_{in} - Z_0}{Z_{in} + Z_0} = \Gamma_{in}, \quad (C3)$$

$$S_{21} = \frac{V_{out} + Z_0 I_{out}}{V_{in} + Z_0 I_{in}} = \frac{2V_{out}}{V_{in} + Z_0 I_{in}}, \quad (C4)$$

where we used the relation $I_{out} = V_{out}/Z_0$ and the value of the input impedance $Z_{in} = V_{in}/I_{in}$; Γ_{in} is the input reflection coefficient, and subscripts *in* and *out* denote the input and output quantities of the JTWPA circuit, i.e., the quantities at the first and last node of the circuit, $n = 1$ and $n = N + 1$, respectively. In the simulations performed in this paper, only the forward transmission S_{21} and the input reflectivity S_{11} are determined, because the current sources driving the signal and pump currents are connected to the JTWPA input only (Fig. 3a). This resembles the practical scenario of signal and pump sources connected to the input of the JTWPA, and a passive load (circulators, filters, further amplifier stages) at the output of the JTWPA. It is worth mentioning, that in the presence of a strong pump wave a JTWPA is a non-reciprocal device, i.e., the forward and backward transmissions of the signal are not

identical, $S_{21} \neq S_{12}$. In the ideal case the signal is amplified only when travelling in forward but not in backward direction.

Typically an amplifier like a JTWPA is embedded in an experimental environment having a characteristic impedance of $Z_0 = 50\Omega$, which we chose as a reference impedance. All *WR-spice* simulations performed in this research use a source (Z_S) and load (Z_L) impedance $Z_S = Z_L = Z_0$. However, the characteristic impedance Z of the JTWPA is generally not purely real-valued but possesses a non-vanishing imaginary part, being a side effect of the engineered periodic loadings. Due to the slight impedance mismatch, $Z \neq Z_0$, there is some ambiguity concerning the definition of two-port power gain of the amplifier. To account for reflections of the signal wave at the amplifier's input and output, the definition of the transducer power gain⁴⁴ is used, which, in the case of $Z_S = Z_L = Z_0$, is

$$G = P_L / P_A = |S_{21}|^2, \quad (C5)$$

where P_L and P_A denote the power at the load and the power available from the source, respectively.

REFERENCES

- ¹R. Movshovich, B. Yurke, P. G. Kaminsky, A. D. Smith, A. H. Silver, R. W. Simon, and M. V. Schneider, Observation of zero-point noise squeezing via a Josephson-parametric amplifier, *Phys. Rev. Lett.* **65**, 1419 (1990).
- ²M. A. Castellanos-Beltran, K. D. Irwin, G. C. Hilton, L. R. Vale, and K. W. Lehnert, Amplification and squeezing of quantum noise with a tunable Josephson metamaterial, *Nat. Phys.* **4**, 929 (2008).
- ³M. Htridge, R. Vijay, D. H. Slichter, J. Clarke, and I. Siddiqi, Dispersive magnetometry with a quantum limited SQUID parametric amplifier, *Phys. Rev. B* **83**, 134501 (2011).
- ⁴R. Vijay, D. H. Slichter, and I. Siddiqi, Observation of Quantum Jumps in a Superconducting Artificial Atom, *Phys. Rev. Lett.* **106**, 110502 (2011).
- ⁵E. Flurin, N. Roch, F. Mallet, M. H. Devoret, and B. Huard, Generating Entangled Microwave Radiation Over Two Transmission Lines, *Phys. Rev. Lett.* **109**, 183901 (2012).
- ⁶Z. R. Lin, K. Inomata, W. D. Oliver, K. Koshino, Y. Nakamura, J. S. Tsai, and T. Yamamoto, Single-shot readout of a superconducting flux qubit with a flux-driven Josephson parametric amplifier, *Appl. Phys. Lett.* **103**, 132602 (2013).
- ⁷U. Vool, S. Shankar, S. Mundhada, N. Ofek, A. Narla, K. Sliwa, E. Zalys-Geller, Y. Liu, L. Frunzio, R. Schoelkopf, S. Girvin, and M. Devoret, Continuous Quantum Nondemolition Measurement of the Transverse Component of a Qubit, *Phys. Rev. Lett.* **117**, 133601 (2016).
- ⁸M. H. Devoret and R. J. Schoelkopf, Superconducting Circuits for Quantum Information: An Outlook, *Science* **339**, 1169 (2013).
- ⁹O. Yaakobi, L. Friedland, C. Macklin, and I. Siddiqi, Parametric amplification in Josephson junction embedded transmission lines, *Phys. Rev. B* **87**, 144301 (2013).
- ¹⁰K. O'Brien, C. Macklin, I. Siddiqi, and X. Zhang, Resonant Phase Matching of Josephson Junction Traveling Wave Parametric Amplifiers, *Phys. Rev. Lett.* **113**, 157001 (2014).
- ¹¹T. C. White, J. Y. Mutus, I.-C. Hoi, R. Barends, B. Campbell, Y. Chen, Z. Chen, B. Chiaro, A. Dunsworth, E. Jeffrey, J. Kelly, A. Megrant, C. Neill, P. J. J. O'Malley, P. Roushan, D. Sank, A. Vainsencher, J. Wenner, S. Chaudhuri, J. Gao, and J. M. Martinis, Traveling wave parametric amplifier with Josephson junctions using minimal resonator phase matching, *Appl. Phys. Lett.* **106**, 242601 (2015).
- ¹²C. Macklin, K. O'Brien, D. Hover, M. E. Schwartz, V. Bolkhovsky, X. Zhang, W. D. Oliver, and I. Siddiqi, A near-quantum-limited Josephson traveling-wave parametric amplifier, *Science* **350**, 307 (2015).
- ¹³M. Bell and A. Samolov, Traveling-Wave Parametric Amplifier Based on a Chain of Coupled Asymmetric SQUIDS, *Phys. Rev. Applied* **4**, 024014 (2015).
- ¹⁴A. Zorin, Josephson Traveling-Wave Parametric Amplifier with Three-Wave Mixing, *Phys. Rev. Applied* **6**, 034006 (2016).
- ¹⁵A. B. Zorin, M. Khabipov, J. Dietel, and R. Dolata, Traveling-Wave Parametric Amplifier Based on Three-Wave Mixing in a Josephson Metamaterial, in *2017 16th International Superconductive Electronics Conference (ISEC)* (2017) pp. 1–3.
- ¹⁶W. Zhang, W. Huang, M. Gershenson, and M. Bell, Josephson Metamaterial with a Widely Tunable Positive or Negative Kerr Constant, *Phys. Rev. Applied* **8**, 051001 (2017).
- ¹⁷A. Miano and O. A. Mukhanov, Symmetric Traveling Wave Parametric Amplifier, *IEEE Trans. Appl. Supercond.* **29**, 1 (2019).
- ¹⁸A. Zorin, Flux-Driven Josephson Traveling-Wave Parametric Amplifier, *Phys. Rev. Applied* **12**, 044051 (2019).
- ¹⁹L. Planat, A. Ranadive, R. Dassonville, J. Puertas Martínez, S. Léger, C. Naud, O. Buisson, W. Hasch-Guichard, D. M. Basko, and N. Roch, Photonic-Crystal Josephson Traveling-Wave Parametric Amplifier, *Phys. Rev. X* **10**, 021021 (2020).
- ²⁰A. Ranadive, M. Esposito, L. Planat, E. Bonet, C. Naud, O. Buisson, W. Guichard, and N. Roch, Kerr reversal in Josephson meta-material and traveling wave parametric amplification, *Nature Communications* **13**, 1737 (2022).
- ²¹A. B. Zorin, Quasi-phasematching in a poled Josephson traveling-wave parametric amplifier with three-wave mixing, *Appl. Phys. Lett.* **118**, 222601 (2021).
- ²²B. D. Josephson, Possible new effects in superconductive tunnelling, *Phys. Lett.* **1**, 251 (1962).
- ²³G. P. Agrawal, *Applications of nonlinear fiber optics*, Optics and photonics (Academic Press, San Diego, 2001).
- ²⁴P. K. Tien, Parametric Amplification and Frequency Mixing in Propagating Circuits, *J. Appl. Phys.* **29**, 1347 (1958).
- ²⁵A. Cullen, Theory of the travelling-wave parametric amplifier, *Proc. IEE Part B: Electron. and Communication Eng.* **107**, 101 (1960).
- ²⁶V. Sivak, N. Frattini, V. Joshi, A. Lingenfelter, S. Shankar, and M. Devoret, Kerr-Free Three-Wave Mixing in Superconducting Quantum Circuits, *Phys. Rev. Applied* **11**, 054060 (2019).
- ²⁷N. E. Frattini, U. Vool, S. Shankar, A. Narla, K. M. Sliwa, and M. H. Devoret, 3-wave mixing Josephson dipole element, *Appl. Phys. Lett.* **110**, 222603 (2017).
- ²⁸N. E. Frattini, V. V. Sivak, A. Lingenfelter, S. Shankar, and M. H. Devoret, Optimizing the Nonlinearity and Dissipation of a SNAIL Parametric Amplifier for Dynamic Range, *Phys. Rev. Applied* **10**, 054020 (2018).
- ²⁹T. Dixon, J. Dunstan, G. Long, J. Williams, P. Meeson, and C. Shelly, Capturing Complex Behavior in Josephson Traveling-Wave Parametric Amplifiers, *Phys. Rev. Applied* **14**, 034058 (2020).
- ³⁰M. Malnou, M. Vissers, J. Wheeler, J. Aumentado, J. Hubmayr, J. Ullom, and J. Gao, Three-Wave Mixing Kinetic Inductance Traveling-Wave Amplifier with Near-Quantum-Limited Noise Performance, *PRX Quantum* **2**, 010302 (2021).
- ³¹M. Perelshtain, K. Petrovnikin, V. Vesterinen, S. H. Raja, I. Lilja, M. Will, A. Savin, S. Simbierowicz, R. Jabdaraghi, J. Lehtinen, L. Grönberg, J. Hassel, M. Prunnila, J. Govenius, S. Paraoanu, and P. Hakonen, Broadband continuous variable entanglement generation using Kerr-free Josephson metamaterial (2021), arXiv:2111.06145 [cond-mat.supr-con].
- ³²J. Clarke and A. I. Braginski, eds., *The SQUID Handbook: Fundamentals and Technology of SQUIDS and SQUID Systems*, 1st ed. (Wiley, 2004).
- ³³S. Zhao and S. Withington, Quantum analysis of second-order effects in superconducting travelling-wave parametric amplifiers, *Journal of Physics D: Applied Physics* **54**, 365303 (2021).
- ³⁴B. Ho Eom, P. K. Day, H. G. LeDuc, and J. Zmuidzinas, A wideband, low-noise superconducting amplifier with high dynamic range, *Nat. Phys.* **8**, 623 (2012).
- ³⁵M. R. Vissers, R. P. Erickson, H.-S. Ku, L. Vale, X. Wu, G. C. Hilton, and D. P. Pappas, Low-noise kinetic inductance traveling-wave amplifier using three-wave mixing, *Appl. Phys. Lett.* **108**, 012601 (2016).
- ³⁶R. P. Erickson and D. P. Pappas, Theory of multiwave mixing within the superconducting kinetic-inductance traveling-wave amplifier, *Phys. Rev. B* **95**, 104506 (2017).
- ³⁷R. D. L. Kronig and W. G. Penney, Quantum mechanics of electrons in crystal lattices, *Proc. R. Soc. London Series A* **130**, 499 (1931).
- ³⁸C. Kittel, *Introduction to solid state physics*, 8th ed. (Wiley, Hoboken, NJ, 2013).

2005).

³⁹T. G. Mackay and A. Lakhtakia, *The Transfer-Matrix Method in Electromagnetics and Optics*, Synthesis Lectures on Electromagnetics (Morgan & Claypool, San Rafael, 2020).

⁴⁰Whiteley Research Inc., WRspice Circuit Simulator, <http://www.wrcad.com/wrspice.html>.

⁴¹S. Ó Peatáin, T. Dixon, P. J. Meeson, J. Williams, S. Kafanov, and Y. A. Pashkin, The Effect of Parameter Variations on the Performance of the Josephson Travelling Wave Parametric Amplifiers (2021), arXiv:2112.07766 [cond-mat.supr-con].

⁴²S. Whiteley, Josephson junctions in SPICE3, IEEE Trans. Magn. **27**, 2902 (1991).

⁴³R. E. Jewett, Josephson junctions in SPICE 2G5, Electronics Research Laboratory internal memoranda, University of California, Berkeley, CA (1982).

⁴⁴D. M. Pozar, *Microwave engineering*, 4th ed. (Wiley, Hoboken, NJ, 2012).

⁴⁵J. Y. Qiu, A. Grimsmo, K. Peng, B. Kannan, B. Lienhard, Y. Sung, P. Krantz, V. Bolkhovsky, G. Calusine, D. Kim, A. Melville, B. M. Niedzielski, J. Yoder, M. E. Schwartz, T. P. Orlando, I. Siddiqi, S. Gustavsson, K. P. O'Brien, and W. D. Oliver, Broadband Squeezed Microwaves and Amplification with a Josephson Traveling-Wave Parametric Amplifier (2022), arXiv:2201.11261 [quant-ph].

⁴⁶W. H. Southwell, Using apodization functions to reduce sidelobes in rugate filters, Applied Optics **28**, 5091 (1989).

⁴⁷H. A. Abu-Safia, A. I. Al-Sharif, and I. O. Abu Aljarayesh, Rugate filter sidelobe suppression using half-apodization, Applied Optics **32**, 4831 (1993).

⁴⁸K. Peng, M. Naghiloo, J. Wang, G. D. Cunningham, Y. Ye, and K. P. O'Brien, Floquet-Mode Traveling-Wave Parametric Amplifiers, PRX Quantum **3**, 020306 (2022).

⁴⁹A. Greco, L. Fasolo, A. Meda, L. Callegaro, and E. Enrico, Quantum model for rf-squid-based metamaterials enabling three-wave mixing and four-wave mixing traveling-wave parametric amplification, Phys. Rev. B **104**, 184517 (2021).

⁵⁰L. Fasolo, A. Greco, E. Enrico, F. Illuminati, R. Lo Franco, D. Vitali, and P. Livreri, Josephson Traveling Wave Parametric Amplifiers as non-classical light source for Microwave Quantum Illumination, Measurement: Sensors **18**, 100349 (2021).

⁵¹V. Gaydamachenko and C. Kissling, Numerical analysis of a three-wave-mixing Josephson traveling-wave parametric amplifier with engineered dispersion loadings - data and WRspice netlist <https://doi.org/10.5281/zenodo.7092947> (2022).